Energy &
Environmental
Science

ROYAL SOCIETY
OF **CHEMISTRY**

PAPER

View Article Online
View Journal

Check for updates

Cite this: DOI: 10.1039/d4ee00750f

Revealing unprecedented cathode interface behavior in all-solid-state batteries with oxychloride solid electrolytes†

Feipeng Zhao, ‡[a] Shumin Zhang,‡[a] Shuo Wang,[c] Carmen M. Andrei,[d] Hui Yuan,[de] Jigang Zhou, [f] Jian Wang,[f] Zengqing Zhuo, [g] Yu Zhong,[h] Han Su,[h] Jung Tae Kim, [a] Ruizhi Yu,[a] Yingjie Gao,[a] Jinghua Guo, [g] Tsun-Kong Sham,[i] Yifei Mo [c] and Xueliang Sun *[ab]

Received 17th February 2024,
Accepted 3rd April 2024

DOI: 10.1039/d4ee00750f

rsc.li/ees

All-solid-state lithium batteries (ASSLBs) are highly desirable for their sustainability, enhanced safety, and increased energy densities. The compatibility between cathodes and solid electrolytes (SEs) is critical for ASSLB electrochemical performance. While the conventional $LiCoO_2$ (LCO) cathode shows structural stability, limitations in the energy density and materials cost prompt exploration of Ni-rich, Co-poor cathodes like lithium nickel cobalt manganese oxide (NCM). However, Ni-rich NCM faces challenges with typical solid electrolytes (*e.g.*, sulfides or oxides), hindering high-energy-density ASSLBs. Our study reveals a unique cathode/electrolyte interface behavior with lithium tantalum oxychloride (LTOC) superionic conductors, favoring Co-less, Ni-rich NCM over LCO. The Ta/Co interaction is identified as a failure mechanism for LTOC/LCO, while a kinetically stabilized interface is achieved with lean-Co cathodes. Beyond the cathode material composition, our study also establishes a correlation between the temperature used for battery testing and both interface reactivity and cell performance. This research provides crucial insights into the innovative design of high-performance ASSLBs based on the promising LTOC oxychloride SEs.

Broader context

As the latest generation of solid electrolytes (SEs), lithium metal oxychlorides can deliver an ultrahigh ionic conductivity of up to 10^{-2} S cm^{-1} that can be comparable to the state-of-the-art sulfide SEs and liquid electrolytes. However, the cathode compatibility between oxychloride SEs and various conventional layered oxide cathode active materials remains ambiguous. Herein, we take lithium tantalum oxychloride (LTOC) as an example to investigate its compatibility with three typical CAMs such as $LiCoO_2$ (LCO), $LiNi_{0.5}Co_{0.2}Mn_{0.3}O_2$ (NCM523), and $LiNi_{0.83}Co_{0.11}Mn_{0.06}O_2$ (NCM83). Unexpectedly, cobalt-less NCM83 is found to be the most compatible with LTOC SEs, because (i) the Co-poor composition of NCM83 relieves the detrimental Co/Ta interaction and (ii) the *in situ* formed passivation layer eliminates the negative effect of thermodynamic instability between the Ni-rich cathode and LTOC. In spite of this, reducing temperature is verified to significantly improve the cycling durability when using LCO or NCM523. Therefore, coupling the cathode composition and working temperature is proposed as a feasible approach to realize kinetically stabilized cathode/oxychloride interfaces. Our study uncovers an unprecedented cathode interface behavior with oxychloride SEs, which will provide important guidance in achieving high-energy-density all-solid-state batteries.

---

[a] *Department of Mechanical and Materials Engineering, Western University, London, ON, N6A 5B9, Canada. E-mail: xsun9@uwo.ca*
[b] *Eastern Institute for Advanced Study, Eastern Institute of Technology, Ningbo, Zhejiang 3150200, P. R. China*
[c] *Department of Materials Science and Engineering, University of Maryland, College Park, MD 20742, USA*
[d] *Canadian Centre for Electron Microscopy, McMaster University, Hamilton, ON, L8S 4M1, Canada*
[e] *Department of Materials Science and Engineering, McMaster University, Hamilton, ON, L8S 4L7, Canada*
[f] *Canadian Light Source Inc., University of Saskatchewan, Saskatoon, SK, S7N 2V3, Canada*
[g] *Advanced Light Source, Lawrence Berkeley National Laboratory, Berkeley, CA 94720, USA*
[h] *State Key Laboratory of Silicon Materials, Key Laboratory of Advanced Materials and Applications for Batteries of Zhejiang Province, School of Materials Science & Engineering, Zhejiang University, Hangzhou 310027, China*
[i] *Department of Chemistry, Western University, London, ON, N6A 5B7, Canada*

† Electronic supplementary information (ESI) available. See DOI: **https://doi.org/10.1039/d4ee00750f**

‡ These authors contributed equally to this work.

Introduction

All-solid-state lithium batteries (ASSLBs) have gained considerable interest due to their potential to enable high energy density and improved safety.[1–3] Solid electrolytes (SEs) are a critical component of ASSLBs, and a significant development of SEs has taken place since the first report on $Li_{10}GeP_2S_{12}$ (LGPS),[4] which exhibited competitive ionic conductivity ($>10^{-2}$ S cm^{-1}) compared to conventional liquid electrolytes.[5–8] Following LGPS, several sulfide-based SEs have been reported to possess ultra-high ionic conductivity.[9–11] However, interface instability at both the anode and cathode interfaces hinders the practical application of sulfide-based ASSLBs.[12–14] Besides pursuing satisfactory ionic conductivities of advanced SSEs for the development of ASSLBs, a considerable amount of research has been devoted to solving those interface challenges in the field of ASSLBs.[8,15–17]

The desirable cathode interface stability appeals to revisit halide-based SEs, particularly the chloride SEs.[18–21] The intrinsically high anodic stability (>4.2 V *vs.* Li^+/Li) of chloride SEs enables high-performance ASSLBs using conventional layered oxide cathode active materials (CAMs).[22] However, the ionic conductivity of chloride SEs has been insufficient (*i.e.*, at the level of 10^{-3} S cm^{-1}),[23,24] until the report on oxychloride SEs.[25,26] Among the reported oxychlorides to date,[25–30] Ta-based oxychlorides (Li–Ta–O–Cl or LTOC) exhibit the highest ionic conductivity of 1.24×10^{-2} S cm^{-1} and demonstrate excellent rate capability with layered oxide cathode materials.[25,26] Nonetheless, with regard to the LTOC oxychloride SE based on the new mixed-anion (Cl and O) chemistry,[28] the understanding of the interface between LTOC and various cathode materials is still very limited. Although the cathode interface between chloride SEs and conventional CAMs is regarded stable, the introduced corner-sharing O in LTOC could influence the interface stability against CAMs. Specifically, all structural O atoms have been verified to be located at joint sites to generate a "Ta–O–Ta" skeleton in the structure of LTOC,[26] which delivers high-degree-of-freedom and benefits to the Li-ion transport *via* broadening the energy landscape.[28,31] Nevertheless, the "flexibility" of the corner-sharing O environment brings about the possibility of decomposing the LTOC to constitute different cathode electrolyte interfaces (CEIs) with various CAMs.

In this work, the interface stability between LTOC and conventional layered oxide CAMs, namely $LiCoO_2$ (LCO), $LiNi_{0.5}Co_{0.2}Mn_{0.3}O_2$ (NCM523), and $LiNi_{0.83}Co_{0.11}Mn_{0.06}O_2$ (NCM83), is investigated. These specific CAMs are chosen because they share a similarly layered crystal structure, but with different contents of transition metal elements (Ni, Co, and Mn). The morphologies of each kind of CAM are suggested in Fig. S1 (ESI†). Similar particle size and polycrystalline feature exclude size and morphology effects on the electrochemical performance.[32,33] As displayed in Scheme 1, it is unexpected to find that Co is more kinetically active than other two transition metals (Ni and Mn) when cycling against the LTOC SE, although the chemical reactivity (thermodynamically) between LTOC and Ni-containing CAMs is considered relatively higher than that of the LTOC/LCO interface. Different from the active Co/Ta interaction at the LTOC/LCO interface, isolated interphase passivation with diacritical reaction boundaries is observed at the LTOC/NCM interfaces. The self-terminating interface reaction of the latter makes the LTOC SE prefer Ni-rich (Co-less) CAMs to achieve high electrochemical

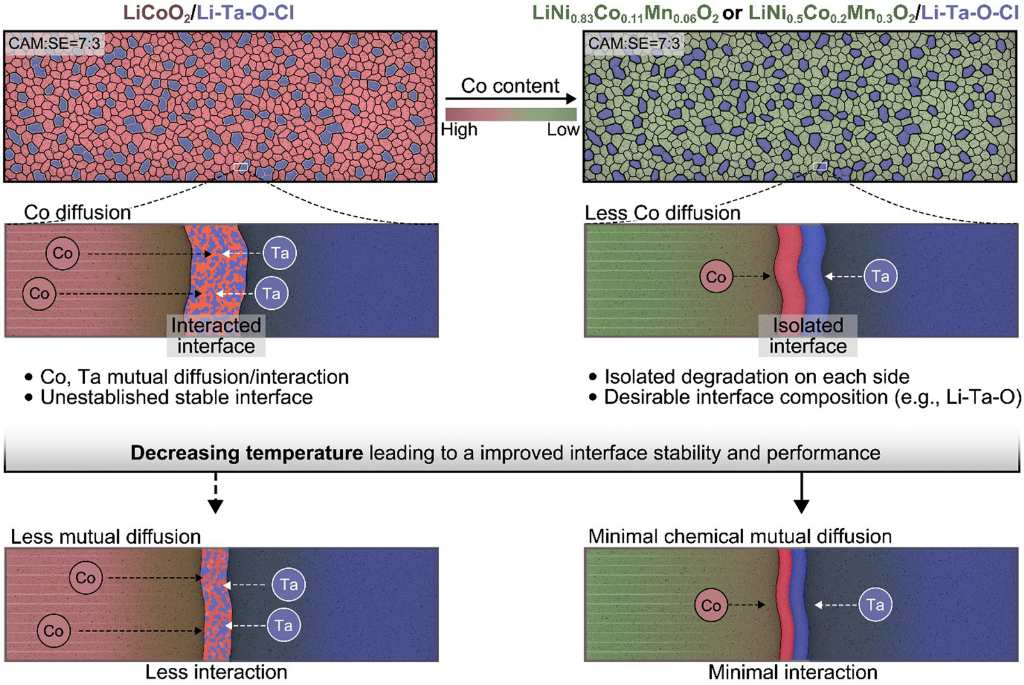

Scheme 1 Illustration on the temperature-dependent interface formation between the Li–Ta–O–Cl (LTOC) SE and conventional cathode materials with different Co contents.

performance at room temperature (RT). In addition, the strategy of reducing the working temperature is effective to suppress the kinetic diffusion of Co at the LTOC/LCO interface, thus improving the cycling stability of LCO solid cells. The low-temperature (LT) control is also verified to decrease the thermodynamic reactivity of LTOC/NCM interfaces, providing us new insights into the design of high-performance ASSLBs.

Results and discussion

Performance of LTOC-based ASSLBs using LCO, NCM523, and NCM83

Ni-rich cathode active materials (CAMs) used in lithium-ion batteries often face structural instability during (de)intercalation when liquid electrolytes are used.[34] However, in an all-solid-state configuration using the LTOC SE, the Ni-rich NCM83 cell exhibited superior stability to the other two selected CAMs, namely LCO and NCM523, as depicted in Fig. 1a. When cycled at RT and 0.2C, the NCM83 solid cell showed a high capacity retention of 96% (calculation relative to the first-cycle capacity and the same after here) after 50 cycles, which was in sharp contrast to the NCM523 (85%) and LCO (78%) cells. The cycling stability for both the LCO and NCM523 solid cells could be improved significantly by simply lowering the cell test temperature (Fig. 1b). When tested at 0.2C and −10 °C, the capacity retentions were maintained as high as 86% and 95% after 200 cycles for the LCO and NCM523 solid cells, respectively. Furthermore, the benefit of lowering operating temperature for the enhanced cycling stability was also verified at current densities of 0.5C and 1C (Fig. S2, ESI†). The improved cycling performance (particularly for the LCO and NCM523 solid cells) through lowering the working temperature is summarized and depicted in Fig. 1c. At other different current densities, ranging from 0.05C to 1C, both LCO (Fig. 1d and e) and NCM523 (Fig. 1f and g) solid cells also demonstrated improved electrochemical reversibility. In contrast, the improvement degree for the NCM83 cell by lowering the operating temperature was subtle (Fig. 1h and i), even though the excellent long-term cycling stability (85% retention after 3000 cycles) was achieved at −10 °C (Fig. S3, ESI†). However, it should be noted that the reversible capacity of all solid cells at −10 °C was decreased at

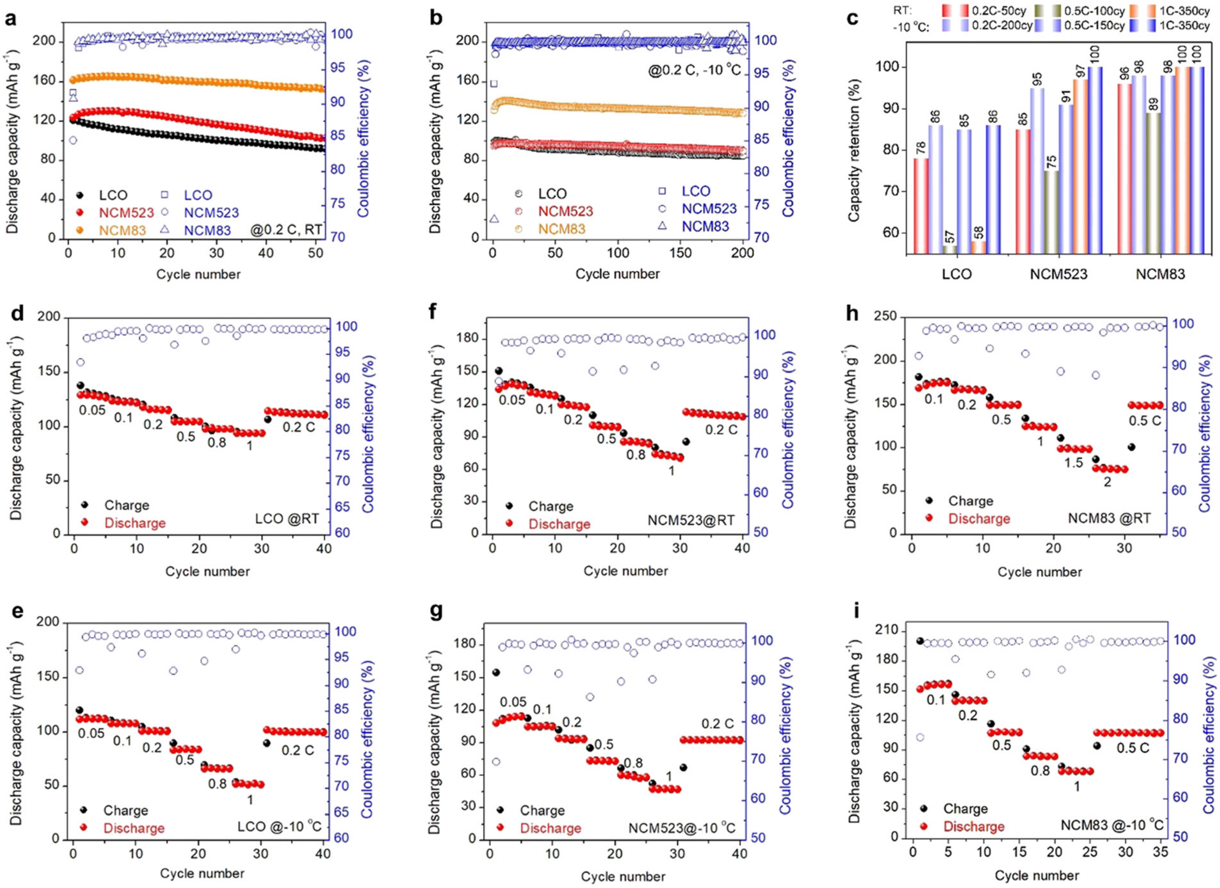

Fig. 1 Electrochemical performance of ASSLBs using the LTOC SE coupling with different CAMs. (a) Cycling stability of using NCM83, NCM523, and LCO at a low current density of 0.2C (RT). (b) Cycling stability of using NCM83, NCM523, and LCO at a low current density of 0.2C and a low temperature of −10 °C. (c) Comparison of the capacity retention after cycling in the solid cells at various current densities (0.2C, 0.5C, and 1C) and temperatures (RT and −10 °C). (d) and (e) Rate capabilities of the LCO cells measured at RT and −10 °C, respectively. (f) and (g) Rate capabilities of the NCM523 cells measured at RT and −10 °C, respectively. (h) and (i) Rate capabilities of the NCM83 cells measured at RT and −10 °C, respectively. Note: the loading mass of CAMs in various solid cells was around 5 mg.

each specific current density due to sluggish electrochemical reaction kinetics of the electrode at low temperatures,[9,35] which resulted in increased polarization during charging and discharging, as indicated in Fig. S4 (ESI†).

Temperature-dependent electrochemical behaviors

As the composition of NCM523 is moderate compared with that of the Co-rich LCO or Ni-rich NCM83, we first used NCM523 as a model CAM to examine the temperature-dependent electrochemical behavior when cycling against the LTOC SE. Variable-rate cyclic voltammetry (CV) measurements were carried out for the NCM523 solid cells at three different temperatures (RT, −10 °C, and 60 °C), as depicted in Fig. 2a–c. Both anodic and catholic peak currents were increased along with elevated scanning rates at RT or −10 °C, but became abnormal at 60 °C when using relatively high scanning rates (over 0.15 mV s^{-1}). Linear fitting of the peak currents for the RT and −10 °C (Fig. 2d and e) derived slopes between 0.5 and 1. It is reported that a slope of 0.5 indicates an ideal situation where a (de)intercalation reaction occurs on the working electrode using layered oxide CAMs.[36] A deviated value towards 1 implies that the uptake of capacity is contributed partially by the Li-ion diffusion process, which is generally dominated by the formation of CEIs.[36] At −10 °C, the anodic slope value (0.56) was much closer to 0.5 than that at RT (0.73), suggesting that the CEI formed at −10 °C showed much less influence than that at RT on the de-intercalation reaction of NCM523 CAMs. This was also verified by collecting the electrochemical impedance spectroscopy (EIS) plots for the NCM523 solid cells cycled (RT and −10 °C) after different cycles (Fig. S5, ESI†). Increasing the temperature to 60 °C deteriorated the CEI stability, because the linear fitting was even not adaptable due to the diverging data points as displayed in Fig. 2f. The similar abnormal redox reaction during the CV measurements occurred on the LCO cell operating at 60 °C, but was greatly eliminated in the NCM83 counterpart (Fig. S6 and S7, ESI†), indicating that the Co content in the CAMs could be as one of the important factors to determine the CEI stability against the LTOC SE. Even so, the increasing temperature was demonstrated to deteriorate the cycling performance of LTOC-based solid cells using these three kinds of CAMs (Fig. S8, ESI†).

Constant current intermittent titration (GITT) measurements were further conducted on the NCM523 solid cells, as

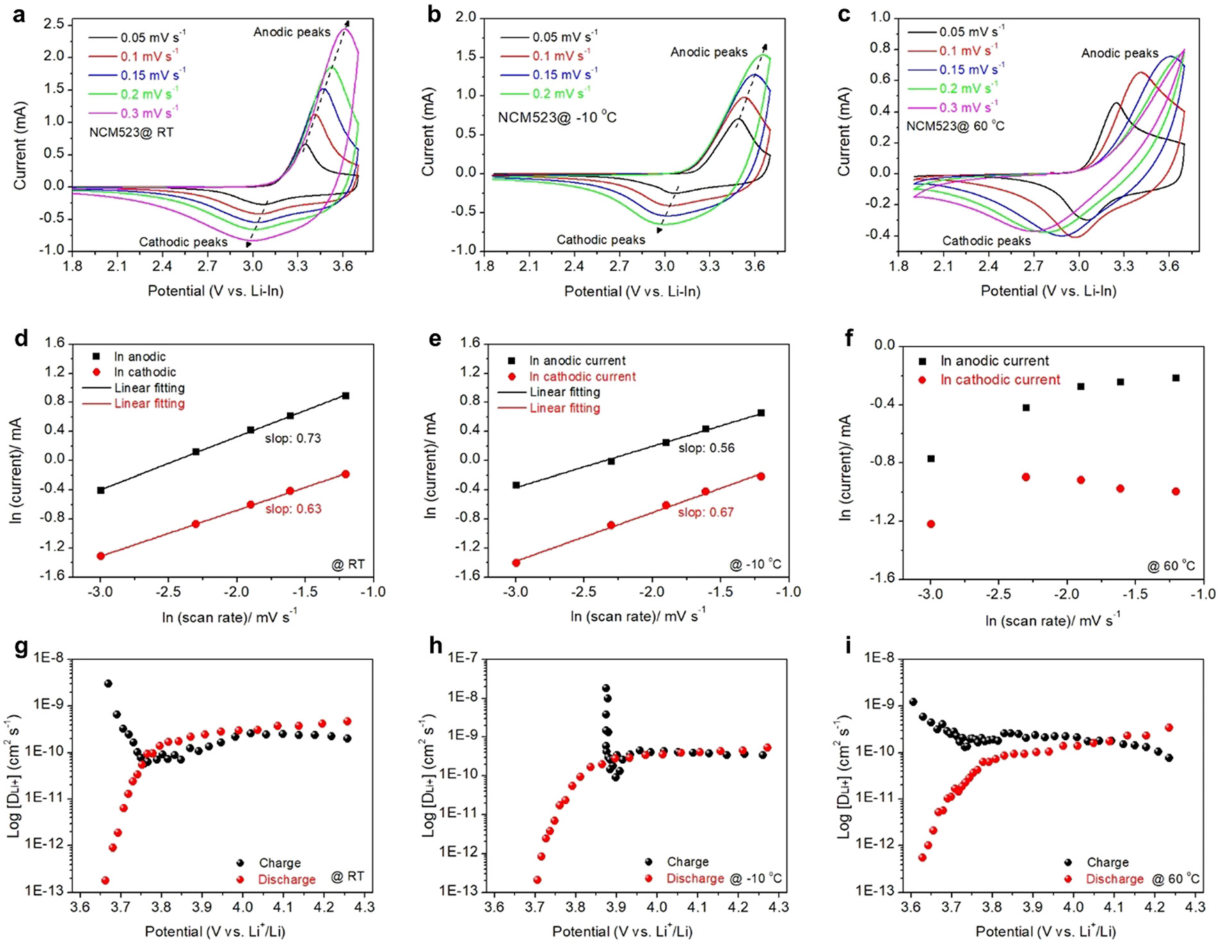

Fig. 2 Temperature-dependent electrochemical behaviors in the NCM523 cells. (a)–(c) CV curves of the NCM523 cells measured at various scan rates at RT, −10 °C (LT), and 60 °C (HT), respectively. (d)–(f) Linear fittings for the scanning rate-dependent cathodic and anodic peak currents from (a)–(c). (g)–(i) Constant current intermittent titration (GITT) measurements on the NCM523 cells performed at 0.1C at RT, −10 °C, and 60 °C, respectively.

shown in Fig. S9 (ESI†). The GITT measurement for the solid cell has been reported that it not only detected the Li-ion relaxation, but also indicated the influence of interface degradation.[37] Derived from the GITT measurements at various temperatures, Li-ion diffusivity in the NCM523 electrode was recorded against the relaxation potential as described in Fig. 2g–i. In the first charging (delithiation) process, high temperature (HT, *i.e.*, 60 °C) brought about faster Li-ion transport in the electrode, showing a higher diffusivity mostly above 10^{-10} cm^2 s^{-1}. Meanwhile, the growth of the CEI at HTs was the most prominent (compared to RT or LT situation). The generated CEI even hindered Li-ion diffusion in the subsequent discharging (lithiation) process, as the Li-ion diffusivity at HT was lower than that in RT during discharging. Additionally, it was shown that in the effective (de)intercalation regions, the LT case presented the highest degree-of-overlap in the diffusivity values during charging and discharging, while the HT case was the worst. These phenomena implied that the LT condition benefited to generate the stabilized CEI and achieved highly reversible (de)intercalation reactions. Similar results were also reported by Janek *et al.* for the sulfide-based ASSLBs,[38] where LT was helpful for stabilizing the interface impedance between LGPS and $LiNi_{0.6}Co_{0.2}Mn_{0.2}O_2$ (NCM622) CAMs, because the interfacial reaction rate constant (k) was exponentially correlated to the temperature.

Characterization on the LTOC/CAMs interfaces

As shown above, the CEI stability between LTOC and CAMs is temperature-dependent, which plays a crucial role in influencing the electrochemical behavior and determining the LTOC-based solid cell performance. To elucidate the interface composition of LTOC/CAMs and the intrinsic reason of the discrepant interface stability using different CAMs, we combined various physicochemical characterization techniques to study LTOC/CAM interfaces. First, thermodynamic calculations provided us the phase equilibria between LTOC and the three CAMs. As shown in Table 1, all three CAMs (NCM83, NCM523, and LCO) are not thermodynamically stable with the LTOC SE, due to the favorable interface reaction.[39,40] In addition to thermodynamic equilibrium, as many theoretical and experimental reports have verified, the inclusion of considering kinetic factors (*e.g.*, interphase passivation layer) at the interface is critical in determining the formation of the CEI and interface stability.[14,41] It has been suggested that the detrimental element mutual diffusion[42] was only observed for the interface of LTOC/LCO leading to the formation of Ta_2CoO_6. Similarly, the Co-involved mutual diffusion was observed at the cathode interface in SSBs based on either sulfide or oxide SSEs.[42,43] For example, inter-diffusion of Co, La, and Zr cations was reported at the interface between LCO and the $Li_7La_3Zr_2O_{12}$ SE with the formation of La_2CoO_4,[43] which was even believed as the starting point of the interface degradation.[44] By contrast, the NCM CAMs with lower Co contents (*i.e.*, NCM523 and NCM83) avoided the formation of the interplayed products at the interface. Instead, the ion-conducting $LiTa_3O_8$ was predicted as one of the reaction products at the interface of LTOC/NCM, which could contribute as a favorable passivation layer of CEIs for Li-ion exchange.[39,45] The interphase discrepancy was also verified by the *in situ* EIS plots recorded in the first charge/discharge process of cycling LCO and NCM83 CAMs, as displayed in Fig. S10 (ESI†). LTOC/LCO interface impedance was continuously increased, while the LTOC/NCM83 showed a much less interface impedance after the first charge/discharge.

Then, the morphologies and chemical distribution details of LTOC/CAM interfaces (after cycling at RT) were obtained experimentally by conducting electron microscopy (EM) characterization. The use of nanosized LTOC SEs effectively enveloped the CAM particles, thus ensuring adequate Li-ion transport pathways, as demonstrated in Fig. S11 and S12 (ESI†). This eliminates any possibility of interface issues arising from a lack of effective physical contact in our analyses. The high-resolution transmission electron microscopy (HRTEM) image of the LTOC/LCO interface revealed that LiCl compounds were embedded in the amorphous matrix (Fig. 3a). The recognition of the LiCl component agreed with the predicted interfacial products above. In addition, Cl was considered rich at the LTOC/LCO interface according to the electron energy loss spectroscopy (EELS) element mapping (Fig. 3b), which affirmed that the interfacial reaction between LTOC and LCO is significant at RT. More interestingly, Co was found diffused deeply across the interface and headed toward the bulk area of LTOC, which was also reflected by the evolution of Co L-edge EELS spectra across the LTOC/LCO interface, as indicated in Fig. 3c. The gradual low-energy shift of the Co L-edge suggested that the oxidation state of Co(III) was reduced, which emerged at the interface and extended to a distance over 100 nm. In sharp contrast, the interface of LTOC/NCM83 showed distinct reaction boundaries as demonstrated in the EELS element mapping (Fig. 3d). Furthermore, as displayed in Fig. 3e, a series of EELS

Table 1 Thermodynamic calculation of the interphase composition between the LTOC SEs and various cathode materials

Cathode	Composition	x_{SE}	Phase equilibria at x_m
LCO	$LiCoO_2$	0.34	Ta_2CoO_6, LiCl, $LiCo_2O_4$, Co_3O_4
	$Li_{0.5}CoO_2$	0.36	Ta_2CoO_6, LiCl, $CoCl_2$, CoO_2
NCM523	$LiNi_{0.5}Co_{0.2}Mn_{0.3}O_2$	0.38	LiCl, $LiTa_3O_8$, $Mn(Ni_3O_4)_2$, $MnNiO_3$, CoO_2
	$Li_{0.5}Ni_{0.5}Co_{0.2}Mn_{0.3}O_2$	0.42	LiCl, Ta_2O_5, O_2, $NiCl_2$, CoO_2, $MnNiO_3$
	$Li_{0.2}Ni_{0.5}Co_{0.2}Mn_{0.3}O_2$	0.64	LiCl, Ta_2O_5, Cl_2, $NiCl_2$, CoO_2, MnO_2
NCM83	$LiNi_{0.83}Co_{0.11}Mn_{0.06}O_2$	0.38	LiCl, $LiTa_3O_8$, O_2, NiO, $Mn(Ni_3O_4)_2$, CoO_2
	$Li_{0.5}Ni_{0.83}Co_{0.11}Mn_{0.06}O_2$	0.62	LiCl, Ta_2O_5, O_2, $NiCl_2$, CoO_2, $MnNiO_3$
	$Li_{0.2}Ni_{0.83}Co_{0.11}Mn_{0.06}O_2$	0.61	LiCl, Ta_2O_5, O_2, $NiCl_2$, CoO_2, $MnNiO_3$

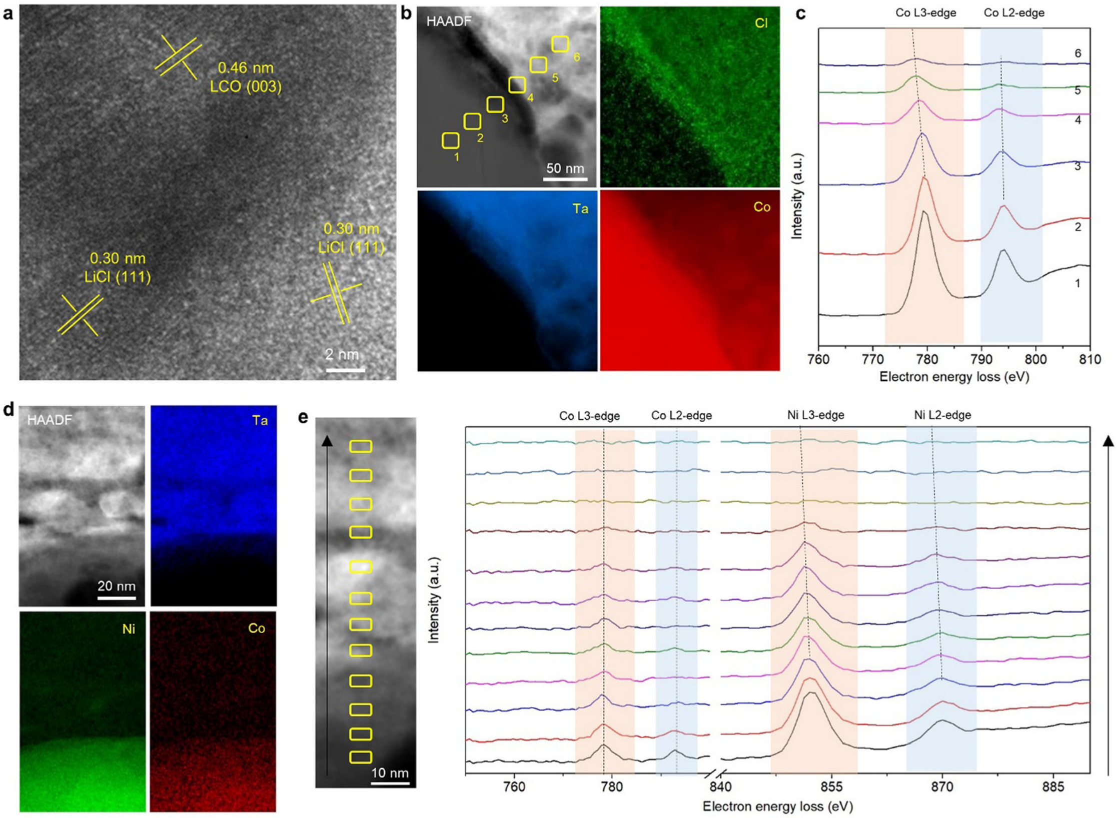

Fig. 3 TEM-EELS characterization on CAM/LTOC interfaces cycled at RT. (a) HRTEM image of the LCO/LTOC interface. (b) High-angle annular dark-field (HAADF) image and EELS element mapping at the LCO/LTOC interface. (c) EELS spectra of the Co L-edge in the marked positions of the HAADF image. (d) HAADF image and EELS element mapping at the NCM83/LTOC interface. (e) HAADF image of the NCM83/LTOC interface and the EELS spectra extracted in selected area across the interface. Note: the interface samples were prepared using a plasma focused ion beam (PFIB) instrument; the EELS scanning step was set as 1 nm.

spectra across the LTOC/NCM83 interface indicated that Co(III) was kept unchanged, but Ni from NCM83 was chemically reduced at the interface. The estimated thickness of the LTOC/NCM83 interface was around 45 nm *via* measuring the penetration depth of reduced Ni species. The transition metal penetration length was significantly lower than that at the LTOC/LCO interface, proving that the LTOC/NCM83 interface was more passivated kinetically. In addition, the element diffusion became serious at an elevated temperature of 60 °C. As shown in Fig. S13 (ESI†), even for the moderate composition of NCM523, the interphase layer could reach ∼150 nm according to the EDS line scan for the FIB-cut cathode sample. Accompanying the chemical reduction of Ni and Ta species (*e.g.*, Ta is possibly in the form of $LiTa_3O_8$ or Ta_2O_5 according to the thermodynamic calculations) showing a higher oxidization state (comparing to Ta in LTOC) could be generated at the LTOC/NCM83 interface. The chemically oxidized (high-energy shift) Ta species were also experimentally confirmed by conducting X-ray photoelectron spectroscopy (XPS) analyses for the cycled LTOC/NCM83 composite as suggested in Fig. S14 (ESI†). In contrast to the distinct chemical evolution of transition metal elements (*i.e.*, Co, Ni, and Ta), O was considered stable at the LTOC/CAM interfaces as displayed in the X-ray absorption spectroscopy (XAS) of O K-edge (Fig. S15, ESI†).

We further employed scanning transmission X-ray microscopy (STXM) to obtain the chemical information of specific CAM particles after cycling against the LTOC SE at various temperatures. One advantage of using STXM compared with only using TEM-EELS is that it can provide higher energy resolution in analyzing the chemistry nature of interfaces.[46,47] As shown in Fig. 4a, the yellow-circled particles were identified as LCO, which was connected to the surrounding LTOC particles. The details about locating CAM particles in the cathode composites are described in Fig. S16 (ESI†). It was found from the series spectra of the Co L-edge (Fig. 4b) that both reduced and oxidized Co(III) species occurred on the cycled LCO particles at RT and HT, while the shape feature of the Co L-edge remained unchanged at LT. The reduced Co(III) might exist in the form of Ta_2CoO_6, Co_3O_4, or $CoCl_2$, while the oxidized Co could be from $LiCo_2O_4$ or CoO_2 (based on the thermodynamic calculations). The suppressed side reaction upon decreasing the test temperature for the LCO solid cells was corresponding to enhanced cycling stability at LT as we discussed in the electrochemistry part. By contrast, the cycled NCM523 and NCM83 particles (RT) identified by the STXM (Fig. S17, ESI†) only showed Co-oxidized components as indicated in Fig. 4c and d, respectively. Thus, echoing to the TEM-EELS results, the chemical activity between Co-rich LCO and LTOC SEs was

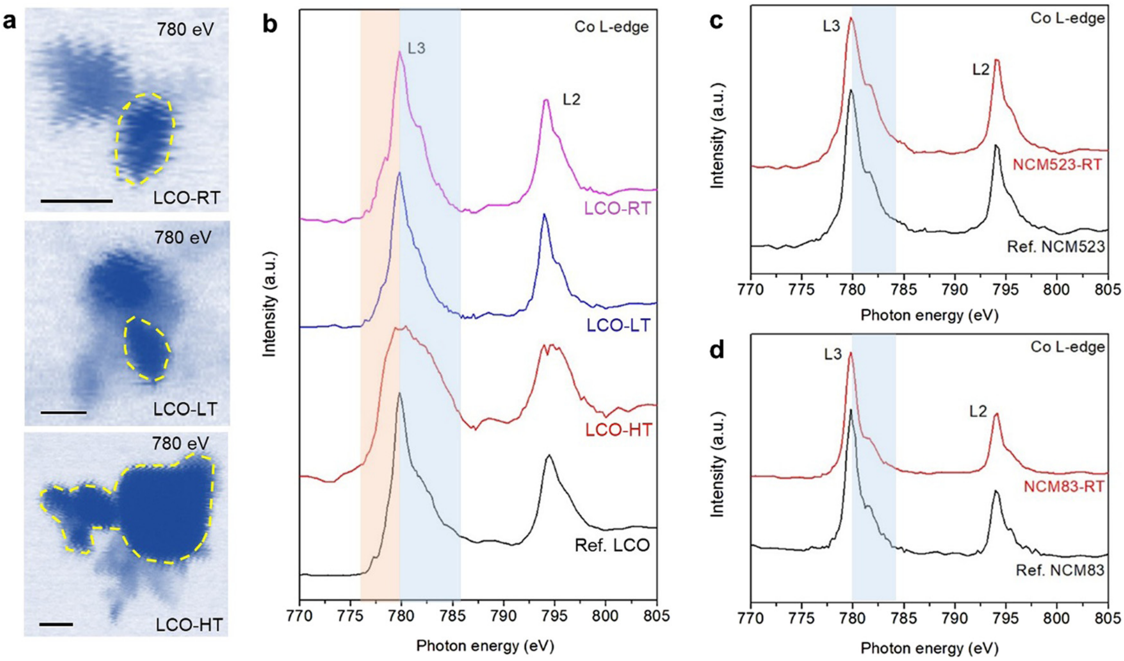

Fig. 4 STXM characterizations on the LTOC/CAM interfaces. (a) LCO particles (circled in yellow) located by STXM at an absorption energy of Co (780 eV). The LCO CAMs were obtained after cycling for 20 cycles at 0.1C and at various temperatures. RT: 25 °C; LT: −10 °C; HT: 60 °C. Scale bar: 500 nm. (b) XAS spectra of the Co L-edge of the identified LCO particles in (a). (c) and (d) XAS spectra of the Co L-edge of the NCM523 and NCM83 particles after cycling (20 cycles, 0.1C and RT), respectively.

experimentally verified, while the LT control demonstrated a feasible approach to reduce the reactivity. Besides, using Co-less NCM CAMs (*i.e.*, NCM523 or NCM83) was confirmed to alleviate the interface reactivity by forming satisfactory interfacial passivation layers.

Conclusions

In this work, we investigated the temperature-dependent electrochemical performance of LTOC-based ASSLBs using three CAMs with varying transition metal compositions: LCO, NCM523, and NCM83. We unexpectedly found that at room temperature, LTOC showed better cycling stability when paired with Ni-rich NCM83 CAMs. However, reducing the temperature significantly improved the cycling durability of LCO and NCM523 CAMs. These results were attributed to the interface stabilities between LTOC and CAMs based on a comprehensive consideration of both thermodynamic and kinetic factors. Our experiments confirmed that the active LTOC/LCO interface is created by kinetically active Co/Ta interaction. However, this negative kinetic effect is alleviated by reducing the working temperature. On the other hand, the LTOC/NCM83 interface is thermodynamically unstable, but is self-evolutionary through the formation of the passivated interphase, which prevents further decomposition. In the case of NCM523, there is still an off-balance between the negative element interaction and the positive passivation. As a result, the electrochemical performance at room temperature is moderate, but there are some improvements in cycling stability when the temperature is reduced. Our study provides insight into how the composition of cathode materials and the working temperature of oxychloride-based ASSLBs can affect the cathode interface stability.

Author contributions

F. Z. and X. S. conceived the project. F. Z. and S. Z. performed the electrolyte synthesis and electrochemical performance characterizations. S. W. performed the computational simulations under the supervision of Y. M. J. W. and J. Z., and Y. G. helped in the STXM measurements and analyses. C. A. and H. Y. helped with EM measurements. J. F. and T. S. suggested on the synchrotron-based data analyses. Z. Z. and J. G. helped with the O K-edge measurements and analyses. Y. Z., H. S., J. T. K., and R. Y. advised the electrochemical characterization. F. Z. and S. Z. formally analyzed all data and wrote the manuscript. X. S. supervised the project. All the authors participated in the reviewing and editing of the manuscript.

Conflicts of interest

There are no conflicts to declare.

Acknowledgements

The authors thank the support from the Natural Sciences and Engineering Research Council of Canada (NSERC), the Canada Research Chair Program (CRC), the Canada Foundation for Innovation (CFI), and the Western University. PFIB and TEM were carried out at the Canadian Centre for Electron Microscopy (CCEM), a national facility supported by the NSERC and McMaster University. The authors acknowledge Sabaa Rashid for her kind help with FIB-SEM characterization. The synchrotron related characterization was completed at the Canadian Light Source (CLS), which is supported by the CFI, the NSERC, the National Research Council (NRC), the Canadian Institutes of Health Research (CIHR), the Government of Saskatchewan, and the University of Saskatchewan. Soft XAS O-K data were obtained using BL7.3.1 of Advanced Light Source (ALS), a U. S. Department of Energy's (DOE's) Office of Science User Facility, under DOE contract no. DE-AC02-05CH11231. Y.M. acknowledges the funding support from the National Science Foundation under the award number 1940166, and the computational facilities from the University of Maryland supercomputing resources.

References

1 J. Janek and W. G. Zeier, *Nat. Energy*, 2023, **8**, 230–240.

2 Q. Zhao, S. Stalin, C.-Z. Zhao and L. A. Archer, *Nat. Rev. Mater.*, 2020, **5**, 229–252.

3 Y. S. Meng, V. Srinivasan and K. Xu, *Science*, 2022, **378**, eabq3750.

4 N. Kamaya, K. Homma, Y. Yamakawa, M. Hirayama, R. Kanno, M. Yonemura, T. Kamiyama, Y. Kato, S. Hama, K. Kawamoto and A. Mitsui, *Nat. Mater.*, 2011, **10**, 682–686.

5 J. W. Liang, X. N. Li, K. R. Adair and X. L. Sun, *Acc. Chem. Res.*, 2021, **54**, 1023–1033.

6 Z. Zhang, Y. Shao, B. Lotsch, Y.-S. Hu, H. Li, J. Janek, L. F. Nazar, C.-W. Nan, J. Maier, M. Armand and L. Chen, *Energy Environ. Sci.*, 2018, **11**, 1945–1976.

7 A. Manthiram, X. Yu and S. Wang, *Nat. Rev. Mater.*, 2017, **2**, 16103.

8 W. Zhao, J. Yi, P. He and H. Zhou, *Electrochem. Energy Rev.*, 2019, **2**, 574–605.

9 Y. Kato, S. Hori, T. Saito, K. Suzuki, M. Hirayama, A. Mitsui, M. Yonemura, H. Iba and R. Kanno, *Nat. Energy*, 2016, **1**, 16030.

10 L. D. Zhou, A. Assoud, Q. Zhang, X. H. Wu and L. F. Nazar, *J. Am. Chem. Soc.*, 2019, **141**, 19002–19013.

11 Y. Seino, T. Ota, K. Takada, A. Hayashi and M. Tatsumisago, *Energy Environ. Sci.*, 2014, **7**, 627–631.

12 Y. Xiao, Y. Wang, S.-H. Bo, J. C. Kim, L. J. Miara and G. Ceder, *Nat. Rev. Mater.*, 2019, **5**, 105–126.

13 R. Chen, Q. Li, X. Yu, L. Chen and H. Li, *Chem. Rev.*, 2019, **120**, 6820–6877.

14 F. Zhao, S. Zhang, Y. Li and X. Sun, *Small Struct.*, 2022, **3**, 2100146.

15 A. M. Nolan, Y. Zhu, X. He, Q. Bai and Y. Mo, *Joule*, 2018, **2**, 2016–2046.

16 A. Banerjee, X. F. Wang, C. C. Fang, E. A. Wu and Y. S. Meng, *Chem. Rev.*, 2020, **120**, 6878–6933.

17 D. H. S. Tan, A. Banerjee, Z. Chen and Y. S. Meng, *Nat. Nanotechnol.*, 2021, **16**, 479.

18 X. N. Li, J. W. Liang, X. F. Yang, K. R. Adair, C. H. Wang, F. P. Zhao and X. L. Sun, *Energy Environ. Sci.*, 2020, **13**, 1429–1461.

19 T. Asano, A. Sakai, S. Ouchi, M. Sakaida, A. Miyazaki and S. Hasegawa, *Adv. Mater.*, 2018, **30**, 1803075.

20 L. Zhou, T.-T. Zuo, C. Y. Kwok, S. Y. Kim, A. Assoud, Q. Zhang, J. Janek and L. F. Nazar, *Nat. Energy*, 2022, **7**, 83–93.

21 K. Tuo, C. W. Sun and S. Q. Liu, *Electrochem. Energy Rev.*, 2023, **6**, 17.

22 S. Wang, Q. Bai, A. M. Nolan, Y. S. Liu, S. Gong, Q. Sun and Y. F. Mo, *Angew. Chem., Int. Ed.*, 2019, **58**, 8039–8043.

23 C. Wang, J. Liang, J. T. Kim and X. Sun, *Sci. Adv.*, 2022, **8**, eadc9516.

24 J. W. Liang, X. N. Li, S. Wang, K. R. Adair, W. H. Li, Y. Zhao, C. H. Wang, Y. F. Hu, L. Zhang, S. Q. Zhao, S. G. Lu, H. Huang, R. Y. Li, Y. F. Mo and X. L. Sun, *J. Am. Chem. Soc.*, 2020, **142**, 7012–7022.

25 Y. Ishiguro, K. Ueno, S. Nishimura, G. Iida and Y. Igarashib, *Chem. Lett.*, 2023, **52**, 237–241.

26 Y. Tanaka, K. Ueno, K. Mizuno, K. Takeuchi, T. Asano and A. Sakai, *Angew. Chem., Int. Ed.*, 2023, **62**, e202217581.

27 K. Wang, Q. Y. Ren, Z. Q. Gu, C. M. Duan, J. Z. Wang, F. Zhu, Y. Y. Fu, J. P. Hao, J. F. Zhu, L. H. He, C. W. Wang, Y. Y. Lu, J. Ma and C. Ma, *Nat. Commun.*, 2021, **12**, 4410.

28 S. Zhang, F. Zhao, J. Chen, J. Fu, J. Luo, S. H. Alahakoon, L.-Y. Chang, R. Feng, M. Shakouri, J. Liang, Y. Zhao, X. Li, L. He, Y. Huang, T.-K. Sham and X. Sun, *Nat. Commun.*, 2023, **14**, 3780.

29 B. Li, Y. Li, H.-S. Zhang, T.-T. Wu, S. Guo and A.-M. Cao, *Sci. China Mater.*, 2023, **66**, 3123–3128.

30 T. Dai, S. Y. Wu, Y. X. Lu, Y. Yang, Y. Liu, C. Chang, X. H. Rong, R. J. Xiao, J. M. Zhao, Y. H. Liu, W. H. Wang, L. Q. Chen and Y. S. Hu, *Nat. Energy*, 2023, **8**, 1221–1228.

31 Z. Z. Zhang and L. F. Nazar, *Nat. Rev. Mater.*, 2022, **7**, 389–405.

32 Y. Han, S. H. Jung, H. Kwak, S. Jun, H. H. Kwak, J. H. Lee, S. T. Hong and Y. S. Jung, *Adv. Energy Mater.*, 2021, **11**, 2100126.

33 X. S. Liu, B. Z. Zheng, J. Zhao, W. M. Zhao, Z. T. Liang, Y. Su, C. P. Xie, K. Zhou, Y. X. Xiang, J. P. Zhu, H. C. Wang, G. M. Zhong, Z. L. Gong, J. Y. Huang and Y. Yang, *Adv. Energy Mater.*, 2021, **11**, 2003583.

34 H. H. Ryu, K. J. Park, C. S. Yoon and Y. K. Sun, *Chem. Mater.*, 2018, **30**, 1155–1163.

35 N. Zhang, T. Deng, S. Zhang, C. Wang, L. Chen, C. Wang and X. Fan, *Adv. Mater.*, 2021, **34**, 2107899.

36 H. Lindstrom, S. Sodergren, A. Solbrand, H. Rensmo, J. Hjelm, A. Hagfeldt and S. E. Lindquist, *J. Phys. Chem. B*, 1997, **101**, 7717–7722.

37 R. Ruess, S. Schweidler, H. Hemmelmann, G. Conforto, A. Bielefeld, D. A. Weber, J. Sann, M. T. Elm and J. Janek, *J. Electrochem. Soc.*, 2020, **167**, 100532.

38 T. T. Zuo, R. Ruess, R. J. Pan, F. Walther, M. Rohnke, S. Hori, R. Kanno, D. Schroder and J. Janek, *Nat. Commun.*, 2021, **12**, 6669.

39 Y. H. Xiao, L. J. Miara, Y. Wang and G. Ceder, *Joule*, 2019, **3**, 1252–1275.

40 A. M. Nolan, Y. S. Liu and Y. F. Mo, *ACS Energy Lett.*, 2019, **4**, 2444–2451.

41 Y. Zhu, X. He and Y. Mo, *ACS Appl. Mater. Interfaces*, 2015, **7**, 23685–23693.

42 A. Sakuda, A. Hayashi and M. Tatsumisago, *Chem. Mater.*, 2010, **22**, 949–956.

43 K. H. Kim, Y. Iriyama, K. Yamamoto, S. Kumazaki, T. Asaka, K. Tanabe, C. A. J. Fisher, T. Hirayama, R. Murugan and Z. Ogumi, *J. Power Sources*, 2011, **196**, 764–767.

44 M. M. Din, L. Ladenstein, J. Ring, D. Knez, S. Smetaczek, M. Kubicek, M. Sadeqi-Moqadam, S. Ganschow, E. Salagre, E. G. Michel, S. Lode, G. Kothleitner, I. Dugulan, J. G. Smith, A. Limbeck, J. Fleig, D. J. Siegel, G. J. Redhammer and D. Rettenwander, *Adv. Funct. Mater.*, 2023, **33**, 2303680.

45 Y. Z. Zhu, X. F. He and Y. F. Mo, *J. Mater. Chem. A*, 2016, **4**, 3253–3266.

46 W. H. Li, Z. Q. Wang, F. P. Zhao, M. S. Li, X. J. Gao, Y. Zhao, J. Wang, J. G. Zhou, Y. F. Hu, Q. F. Xiao, X. Y. Cui, M. J. Eslamibidgoli, M. H. Eikerling, R. Y. Li, F. Brandys, R. Divigalpitiya, T. K. Sham and X. L. Sun, *Chem. Mater.*, 2020, **32**, 1272–1280.

47 A. E. Goode, A. E. Porter, M. P. Ryan and D. W. McComb, *Nanoscale*, 2015, **7**, 1534–1548.